Giant piezoelectricity on Si for hyper-active MEMS

S. H. Baek[1], J. Park[2], D. M. Kim[1], V. Aksyuk[3], R. R. Das[1], S. D. Bu[1], D. A. Felker[4], J. Lettieri[5], V. Vaithyanathan[5], S. S. N. Bharadwaja[5], N. Bassiri-Gharb [5], Y. B. Chen[6], H. P. Sun[6], C. M. Folkman[1], H. W. Jang[1], D. J. Kreft[2], S. K. Streiffer[7], R. Ramesh[8], X. Q. Pan[6], S. Trolier-McKinstry[5], D. G. Schlom[5,9], M. S. Rzchowski[3], R. H. Blick[2], C. B. Eom[1*]

[1]*Department of Materials Science and Engineering, University of Wisconsin, Madison, WI 53706*

[2]*Department of Electrical and Computer Engineering, University of Wisconsin-Madison, Madison, WI 53706*

[3]*Center for Nanoscale Science and Technology, National Institute of Standards and Technology, Gaithersburg, MD 20899*

[4]*Department of Physics, University of Wisconsin, Madison, WI 53706*

[5]*Department of Materials Science and Engineering, Penn State University, University Park, PA 16802*

[6]*Department of Materials Science and Engineering, University of Michigan, Ann Arbor, MI 48109*

[7]*Center for Nanoscale Materials, Argonne National Laboratory, Argonne, IL 60439*

[8]*Department of Materials Science and Engineering, University of California, Berkeley, CA 94720*

[9]*Department of Materials Science and Engineering, Cornell University, Ithaca, NY 14853-1501*

[*]To whom correspondence should be addressed. E-mail: eom@engr.wisc.edu

Microelectromechanical systems (MEMS) incorporating active piezoelectric layers offers integrated actuation, sensing, and transduction. The broad implementation of such active MEMS has long been constrained by the inability to integrate materials with giant piezoelectric response, such as $Pb(Mg_{1/3}Nb_{2/3})O_3$-$PbTiO_3$ (PMN-PT). We synthesized high-quality PMN-PT epitaxial thin films on vicinal (001) Si wafers using an epitaxial (001) $SrTiO_3$ template layer, with superior piezoelectric coefficients ($e_{31,f}$ = -27 ± 3 C/m^2) and figures of merit for piezoelectric energy harvesting systems. We have incorporated these heterostructures into microcantilevers that are actuated with extremely low drive voltage due to thin-film piezoelectric properties that rival bulk PMN-PT single crystals. These epitaxial heterostructures exhibit very large electromechanical coupling for ultrasound medical imaging, micro-fluidic control, mechanical sensing and energy harvesting.

Silicon is the gold standard for microelectronic devices as well as for micro-electromechanical systems (MEMS). However, the main drawback in the world of MEMS is that silicon (Si) is a passive material, i.e. it takes metallic electrodes to capacitively displace MEMS. On the other hand active piezoelectric materials such as lead zirconate titanate (PZT) offer the integration of mechanical displacement (*1-5*). The highest performing piezoelectric MEMs heterostructures, including energy-harvesting devices and actuator structures, have been fabricated with lead zirconate titanate (PZT) piezoelectric layers. A. K. Sharma *et al*. first demonstrated the integration of epitaxial lead zirconate titanate (PZT) thin films on Si substrates using a $SrTiO_3$/MgO/TiN buffer layer (*6*). Subsequent work further enhanced PZT thin-film piezoelectric properties, and demonstrated high functionality active piezoelectric devices incorporating PZT on Si (*3-8*).

Relaxor ferroelectrics with engineered domain states have dramatically enhanced piezo-response over PZT. $Pb(Mg_{1/3}Nb_{2/3})O_3$-$PbTiO_3$ (PMN-PT), one of the lead-based relaxor-ferroelectrics, exhibits strain levels and piezoelectric coefficients that can be five to ten times those of PZT, and has a large electromechanical coupling coefficient of k_{33} ~0.9 (*9, 10*). Performance of piezoelectric MEMs could be enhanced dramatically by incorporating these materials. This requires the integration of PMN-PT films with Si, while preserving their enhanced piezoelectric properties. This has been an unrealized goal for 15 years. Here, we present an approach in which oxide heteroepitaxy on silicon is used to preserve the phase purity and properties of PMN-PT films.

Integration of high piezoelectric coefficient PMN-PT films on Si substrates has been pursued for more than a decade, but without achieving large increases in piezoelectric response over materials such as PZT. The piezoelectric properties of relaxor-ferroelectrics depend on both

intrinsic (stoichiometry, orientation), and processing-related factors (phase purity, defect density). In many ferroelectric solid solutions, the physical properties are maximized at the morphotropic phase boundary (MPB), which occurs at 33 % PT in the PMN-PT solid solution system (*10*). In rhombohedral or MPB PMN-PT, $(001)_{pc}$ oriented single crystals provide large, non-hysteretic piezoelectric coefficients compared to $(111)_{pc}$ oriented ones (*9*) (the subscript "pc" stands for pseudocubic). One of the major difficulties is the appearance of a pyrochlore phase; a multi-step Columbite process was developed to bypass the pyrochlore phase in bulk PMN-PT ceramics where pre-reacting magnesium and niobium oxides are used to react with lead oxide (PbO) (*11*). However, such a method is not applicable to thin film synthesis. Thus, thin film growth conditions must be carefully controlled in order to achieve $(001)_{pc}$ oriented single crystal PMN-PT films.

To stabilize the perovskite phase and achieve epitaxial growth of the desired orientation, we have implemented two approaches: (1) using an epitaxial $SrTiO_3$ buffer layer and (2) a miscut Si substrate. The latter approach works well for growing phase-pure thin films of oxide materials with volatile constituents (*12, 13*). We believe that the effect of high density of steps on the surface of miscut substrates is to maintain film stoichiometry, by effectively incorporating volatile constituents (such as PbO) into the film, suppressing formation of pyrochlore, which is lead-deficient. The (001) epitaxial $SrTiO_3$ layer on Si, deposited by reactive molecular-beam epitaxy (MBE), enables us to grow single crystal $(001)_{pc}$ PMN-PT layer on epitaxial $(001)_{pc}$ $SrRuO_3$ bottom electrodes using the control provided by heteroepitaxy. The conventional method showed that the structural quality of the $SrTiO_3$ was degraded as the orientation of the silicon wafers deviated from exact (001) orientation due to the high density of steps and the increased reactivity of exposed Si step edges (*14, 15*). Such significant growth challenges were overcome

to grow high quality $SrTiO_3$ on miscut Si (*16*). The phase purity, crystal structure, and epitaxial arrangements of 3.5 μm thick PMN-PT / $SrRuO_3$ / $SrTiO_3$ / Si were studied using a four-circle x-ray diffractometer with both a two-dimensional area detector and a four-bounce monochromator. Fig. 1A and 1B show the θ-2θ scans of 3.5 μm thick PMN-PT films grown under the same conditions on exact (±0.1°) and 4° miscut Si substrates, respectively. The PMN-PT film on exact Si exhibits a large volume of pyrochlore phase as well as polycrystalline perovskite phase. In contrast, the PMN-PT film on 4° miscut Si shows a dramatic improvement in terms of both phase purity and epitaxy of perovskite phase. It has no detectable pyrochlore phase.

Azimuthal ϕ scans of this phase-pure PMN-PT film, Fig. 1C, show in-plane epitaxy with a cube-on-cube epitaxial relationship, $[100]_{pc}$ PMN-PT // $[100]_{pc}$ $SrRuO_3$ // [100] $SrTiO_3$ // [110] Si. The full width at half maximum (FWHM) of the 002_{pc} ω scan, and of the 101_{pc} ϕ scan are 0.26° and 0.6°, respectively. Commercial PMN-PT bulk single crystals have FWHM of 0.14° and 0.27°, respectively. Transmission electron microscopy (TEM) analysis also confirms epitaxial growth of the PMN-PT heterostructure on Si. Fig. 1D is a low magnification bright-field TEM image. The inset is the selected-area electron diffraction (SAED) pattern taken from the PMN-PT layer along the $[010]_{pc}$ zone axis. The high-resolution TEM image (Fig. 1E) exhibits an atomically sharp interface between the $SrRuO_3$ and PMN-PT layers; the epitaxial match between the layers is clear. Also, chemical composition analysis by wavelength dispersive spectroscopy (WDS) shows that the PMN-PT films are stoichiometric with 0.67PMN-0.33PT composition within experimental error. These analyses confirm that PMN-PT thin films on miscut Si in this work are stoichiometric, phase-pure, $(001)_{pc}$ oriented single crystals.

The polarization versus electric field (*P*-*E*) hysteresis loops were measured for 1 μm-thick PMN-PT films on Si (Fig. 2A). We observe that the *P*-*E* loops are negatively imprinted,

indicating the existence of a built-in bias of magnitude –38 kV/cm. As shown in Fig. 2B, the dielectric constant and loss versus electric field measurement exhibits the same negative shift. This has a number of important consequences. First, the built-in bias increases the magnitude of the remanent polarization (P_r). Typically, a compressive in-plane stress results in a counterclockwise rotation of the *P-E* loops of perovskite ferroelectrics, increasing the measured remanent polarization, while in-plane tensile stresses act in the opposite way (*17*). Because of the difference of thermal expansion coefficients between PMN-PT and Si, PMN-PT films on silicon are typically under a tensile strain, decreasing their P_r. Here, the preferred polarization direction (imprint) displaces the somewhat tilted hysteresis loop, increasing the positive remanent polarization to ≈19 μC/cm^2, which in turn increases the piezoelectric response at zero-applied field. Secondly, the built-in bias stabilizes the polarization of PMN-PT in a certain direction, for these films, downward. As a result, piezoelectric devices built from these films should show significantly less aging in the piezoelectric response (*18*), and will be more robust against depolarization due to voltage or temperature excursions (*19*). This mitigates one of the known problems with undoped PMN-PT single crystals, that the low coercive field limits the reverse drive voltages that can be applied. The high levels of imprint achieved here exceed those reported for Mn and Zr-doped PMN-PT crystals (*20*). Thirdly, the built-in bias decreases the permittivity at zero field as shown in Fig. 2B. This increases the figure of merit for sensors operating in a voltage sensing mode, as well as piezoelectric energy harvesting systems. One contribution to the built-in bias arises from the asymmetry of the top and bottom electrodes (*16*).

The effective transverse piezoelectric coefficients $e_{31,f}$ were obtained using a modified wafer flexure method (*21*). The induced charge was measured while subjecting the 1 μm thick PMN-PT films to a cyclic ac strain in order to obtain $e_{31,f}$. The $e_{31,f}$ coefficient is the material's

figure of merit for the majority of micromachined piezoelectric charge-based sensors as well as actuators (*3-5*), enabling performance comparisons between systems of different detailed geometries. The significant self polarization translated into high $e_{31,f}$ coefficients (from -12 C/m^2 to -22 C/m^2 ± 3 C/m^2) for the as-deposited PMN-PT films. After short poling steps, the highest $e_{31,f}$ measured was –27 C/m^2 ± 3 C/m^2. Fig. 2C compares these PMN-PT $e_{31,f}$ values to a wide range of previous work, demonstrating that these are the highest reported for any piezoelectric thin films. This translates directly to a reduction in the required driving voltage for piezoelectric MEMS actuators. As an example, replacing the randomly oriented PZT actuators in the radio frequency (RF) MEMS switches reported in Ref. 19 with these PMN-PT films would decrease the voltage required to minimize contact resistance from ≈ (8 to 10) V to ≤2.5 V. This, in turn, enables actuators which can be driven by low voltage CMOS circuits with high actuation authority. We have confirmed this figure of merit analysis with comparative numerical modeling of PZT and PMN-PT actuators of similar geometries (*16*).

In addition to the large $e_{31,f}$ values, the PMN-PT films also provide large values for $\frac{e_{31,f}^2}{\varepsilon_r}$, where ε_r is the dielectric permittivity, a figure of merit useful for energy harvesting heterostructures in which most of the elastic energy is stored in the non-piezoelectric layers (*22-25*). Fig. 2C compares our films figure of merit with PZT and other piezoelectric materials, demonstrating the advantages of these PMN-PT films for energy-harvesting applications. We have confirmed these improved responses with comparative simulations of an end-loaded PMN-PT and PZT cantilevers using a self-consistent data set (*16*). The high figure of merit observed here is a consequence both of the large piezoelectric response and of the imprint in the hysteresis loop, which reduces the permittivity at zero applied field. Note that in cases where the elastic

energy is stored primarily in the piezoelectric, a more useful figure of merit is $\frac{e_{31,f}^2}{\varepsilon_r Y}$, where Y is Young's modulus. Given the comparable Young' modulus between PMN-PT (115 Gpa) (*25*) and PZT (100 ~ 150 GPa) (*26-28*), PMN-PT still shows at least twice higher figure of merit than the best PZT reported in this case.

It is also important to verify that these large piezoelectric coefficients are not degraded by the microfabrication process. In order to check this, we have fabricated PMN-PT cantilevers, a prototypical structure for electromechanical devices using the e_{31} mode. The resulting behavior was then compared with a model based on parameters from single crystal PMN-PT. Fig. 3A shows the scanning electron microscopy (SEM) image of a cantilever with Pt (60 nm) / PMN-PT (270 nm) / $SrRuO_3$ (100 nm) / $SrTiO_3$ (13 nm) fabricated by conventional microfabrication techniques (*16*). The motion of the PMN-PT cantilevers was characterized by white light interferometry while applying DC or AC voltages across the top and bottom electrodes as shown in Fig. 3B. These measurements were performed at room temperature and ambient pressure.

Fig. 3C shows the measured profile of a 34 μm long cantilever as a function of applied voltage. Note that all the cantilevers are bent downward after release from the Si substrate. This is attributed to the relaxation of the epitaxial strain between PMN-PT (a_{pc}= 0.402 nm) and $SrRuO_3$ (a_{pc}= 0.393 nm). When an electric field is applied parallel to the remanent polarization *i.e.*, a positive voltage is applied on top electrode, the PMN-PT contracts laterally. The vertical displacement arises from bending of the cantilever due to the structural asymmetry between the top (60 nm Pt) and bottom (≈110 nm $SrRuO_3/SrTiO_3$) layers. Fig. 3D shows the tip displacement of the cantilever as a function of the applied voltage. The tip moves 0.375 μm/V ± 0.005 μm/V as shown in the inset of Fig. 3D. Finite element simulation was performed using the

material parameters reported for bulk single crystal PMN-0.33PT from Ref. 25 (*16*). The experimental and modeled results are consistent, as shown by black and red lines in Fig. 3D, respectively. Note that the actual displacement of cantilever also depends on geometry, for example, the thickness of passive layer beneath piezoelectric layer (*29*). Here, we emphasize that high piezoelectric coefficients are still manifested in the devices made from the PMN-PT films.

A commonly used technique for actuating MEMS devices is electrostatics, which is straightforward to implement as it requires only reasonable conductivity of the device structural materials (*2*). A major drawback, however, of electrostatic actuation is the required high control voltage, which places a serious demand on the drive electronics, often preventing scaling down and denser integration of the electronic drivers for actuator arrays. Piezoelectric actuation significantly lowers the driving voltage while achieving the same displacement. The simulation exhibits that an electrostatic cantilever with comparable geometry to our PMN-PT cantilever requires much higher voltages for similar displacement, as shown in Fig. 3D (*16*).

The strong piezoelectric activity of these PMN-PT thin films will dramatically enhance the freedom of designing small electromechanical devices with better performance. They can provide a wide range of piezoelectric device applications such as ultrasound medical imaging, micro-fluidic control, piezotronics and energy harvesting. The geometries fabricated and discussed here take advantage of the 31 piezoresponse. Devices with PMN-PT thin films exploiting the 33 response (*22*) would also benefit from the enhanced piezo response of PMN-PT over PZT, and also from the higher coupling factor in the 33 mode (*23*). Although technically challenging for thin films, shear-mode based structures would also benefit (*30*). Silicon on insulator (SOI) substrates will enable more complex device structures with precisely controlled passive layer thicknesses to control stiffness and displacement. Beyond electromechanical

devices, epitaxial heterostructures with giant piezoelectricity will open a new avenue to tune and modulate multifunctional properties such as ferroelectric, ferromagnetic, superconducting, and multiferroic materials by dynamic strain control (*31, 32*).

References and Notes

1. Uchino, K. *Piezoelectric actuators and ultrasonic motors* (Kluwer Academic, Boston, 1996).

2. J. Judy, *Smart Mater. Struct.* **10**, 1115-1134 (2001).

3. S. Trolier-McKinstry, P. Muralt, *J. Electroceram.* **12**, 7-17 (2004).

4. P. Muralt, *J. Am. Ceram. Soc.* **91**, 1385-1396 (2008).

5. P. Muralt, R. Polcawich, S. Trolier-McKinstry, *MRS Bull.* **34**, 658-664 (2009).

6. A. K. Sharma, J. Narayan, C. Jin, A. Kvit, S. Chattopadhyay, C. Lee, *Appl. Phys. Lett.* **76**, 1458-1460 (2000).

7. M. D. Nguyen, H. N. Vu, D. H. A. Blank, G. Rijnders, *Adv. Nat. Sci.: Nanosci. Nanotechnol.* **2**, 015005 (2011).

8. D. Isarakorn *et al*., *J. Micromech. Microeng.* **20**, 055008 (2010).

9. S. E. Park, T. R. Shrout, *J. Appl. Phys.* **82**, 1804-1811 (1997).

10. S. E. Park, T. R. Shrout, *IEEE Trans. Ultrason. Ferroelectr. Freq. Control* **44**, 1140-1147 (1997).

11. S. L. Swartz and T. R. Shrout, *Mat. Res. Bull.* **17**, 1245-1250 (1982).

12. S. Bu *et al.*, *Appl. Phys. Lett.* **79**, 3482-3484 (2001).

13. R. R. Das *et al.*, *Appl. Phys. Lett.* **88**, 242904 (2006).

14. J. Lettieri, *Critical Issues of Complex, Epitaxial Oxide Growth and Integration with Silicon by Molecular Beam Epitaxy*. http://etda.libraries.psu.edu/theses/approved/WorldWideIndex/ETD-202/index.html (Pennsylvania State University, University Park, 2002)

15. Liang, Y. *et al.* Heteroepitaxy of $SrTiO_3$ on vicinal Si(001): Growth and kinetic effects. *J. Appl. Phys.* **96**, 3413-3416 (2004)

16. Materials and methods are available as supporting material on Science Online.

17. Z. Zhang, J. H. Park, S. Trolier-McKinstry, *MRS Proc. Ferroelectric Thin Films VIII* **596**, 73-77 (2000).

18. R. G. Polcawich and S. Trolier-McKinstry, *J. Mater. Res*. **15,** 2505-2513 (2000).

19. R. G. Polcawich *et al.*, *IEEE T-MTT.* **55,** 2642–2654 (2007).

20. S. J. Zhang, S. M. Lee, D. H. Kim, H. Y. Lee, T. R. Shrout, *Appl. Phys. Lett.* **93** 122908 (2008).

21. J. F. Shepard Jr, P. J. Moses, S. Trolier-McKinstry, *Sens. Actuators.* **71**, 133-138, (1998).

22. N. E. duToit, B. L. Wardle, S. G. Kim, *Integr. Ferroelectr.* **71**, 121-160, (2005).

23. K. A. Cook-Chennault, N. Thambi, A. M. Sastry, *Smart Mater. Struct.* **17,** 043001 (2008).

24. R. Elfrink *et al*., *J. Micromech. Microeng*. **19**, 094005 (2009).

25. R. Zhang, B. Jiang, W. Cao, *J. Appl. Phys*. **90**, 3471-3475 (2001).

26. P. Delobelle, E. Fribourg-Blanc, and D. Remiens, *Thin Solid Films,* **515**, 1385-1393 (2006).

27. T. H. Fang, S. R. Jian, and D. S. Chuu, *J. Phys.-Condens. Matter* **15**, 5253-5259 (2003).

28. H. P. Wu, L. Z. Wu, Q. Sun, W. D. Fei, S. Y. Du, *Appl. Surf. Sci.* **254**, 5492-5496 (2008).

29. P. Muralt *et al*., *IEEE Trans. UFFC*. **52**, 2276-2288 (2005).

30. Bo Ren, Siu Wing Or, Yaoyao Zhang, Qinhui Zhang, Xiaobing Li, Jie Jiao, Wei Wang, Da'an Liu, Xiangyong Zhao, and Haosu Luo, Appl, Phys. Lett. **96**, 083502 (2010)

31. M. Biegalski, K. Dorr, D. Kim, H. Christen, *Appl. Phys. Lett.* **96**, 151905 (2010).

32. L. Pellegrino *et al*., *Adv. Mater.* **21**, 2377-2381 (2009).

33. M. A. Dubois, P. Muralt, *Appl. Phys. Lett.* **74**, 3032-3234 (1999).

34. M. Abazari, A. Safari, S. S. N. Bharadwaja, S. Trolier-McKinstry, *Appl. Phys. Lett.* **96**, 082903 (2010).

35. K. Shibata, *et al*., *Appl. Phys. Exp*. **1**, 011501 (2008).

36. J. H. Park, S. Trolier-McKinstry, *J. Appl. Phys*. **89**, 568-574 (2001).

37. R. A. Wolf, S. Trolier-McKinstry, *J. Appl. Phys*. **95**, 1397-1406 (2004).

38. F. Griggio, S. Trolier-McKinstry, *J. Appl. Lett*. **107**, 024105 (2010).

39. N. Ledermann *et al*., *Sens. Actuators, A* **105**, 162-170 (2003).

40. F. Calame, P. Muralt, *Appl. Phys. Lett*. **90**, 062907 (2007).

Supporting Online Materials

SOM text

Figs. S1 to S4

Tables. S1 to S4

References

Acknowledgements

This work was supported by the National Science Foundation under grant No. ECCS-0708759, and a David Lucile Packard Fellowship (CBE). Work at Penn State was supported by a National Security Science and Engineering Faculty Fellowship. The work was partly supported by a MURI through the Air Force Office for Scientific Research under grant No. FA9550-08-1-0337 (RHB). Work at Argonne National Laboratory and use of the Center for Nanoscale Materials was supported by the U. S. Department of Energy, Office of Science, Office of Basic Energy Sciences, under Contract No. DE-AC02-06CH11357. Work at Cornell was supported by AFOSR through Award No. FA9550-10-1-0524.

Figure captions

Fig. 1 Phase-pure, $(001)_{pc}$-oriented epitaxial PMN-PT thin film on a $SrTiO_3$-buffered Si substrate. X-ray diffraction pattern measured using a 2-dimensional area detector of PMN-PT heterostructure on (001) Si substrates with **(A)** zero miscut ($\pm 0.1^o$) and **(B)** 4^o miscut along [110]. The pyrochlore phase was identified as $Pb_2Nb_2O_7$. Pseudo-cubic notations are used for both PMN-PT and $SrRuO_3$ peak indexing. **(C)** ϕ-scan of the 101_{pc} PMN-PT and 202 Si diffraction peaks. **(D)** Bright-field cross-sectional transmission electron microscopy (TEM) image near the interface between PMN-PT and $SrRuO_3$. The inset is the selective area electron diffraction (SAED) image of PMN-PT along the [100] zone axis. **(E),** High-resolution TEM image of PMN-PT and $SrRuO_3$ interface.

Fig. 2. Dielectric and piezoelectric properties of the PMN-PT film. **(A)** Polarization versus electric field measurement on 1 μm PMN-PT thin film on Si. **(B)** The dielectric constant versus electric field measurement at 1 kHz with a 30 mV oscillating voltage. **(C)** Comparison of figure of merit for micromachined actuators ($e_{31,f}$) and energy harvestors ($e_{31,f}^2/\varepsilon_r$) of PMN-PT film from this work with other reported values: from left AlN (*33*), $Bi_{0.5}Na_{0.5}TiO_3$-$Bi_{0.5}K_{0.5}TiO_3$-$BaTiO_3$ (*34*), $K_{0.5}Na_{0.5}NbO_3$ (*35*), $0.65Pb(Mg_{0.33}Nb_{0.67})$-$0.35PbTiO_3$ (*36*), Random $Pb(Zr,Ti)O_3$ (*37*), (001) $0.3Pb(Ni_{0.33}Nb_{0.67})O_3$-$0.7Pb(Zr_{0.45}Ti_{0.55})O_3$ (*38*), (001) $Pb(Zr_{0.52}Ti_{0.48})O_3$ (*39*), and gradient-free (001) $Pb(Zr_{0.52}Ti_{0.48})O_3$ (*40*).

Fig. 3. Fabrication and characterization of PMN-PT micro-cantilevers. **(A)** Scanning electron microscopy (SEM) image of PMN-PT cantilever. **(B)** Schematic illustration of measurement set-up. Both DC and AC field can be applied between top and bottom electrodes. **(C)** PMN-PT cantilever profile as a function of voltage. **(D)** Tip displacement of 34 μm long cantilever versus applied DC voltage. The inset is the linear scale of tip displacement. The dotted red line is the simulation result for a PMN-PT cantilever with the same geometry. The blue dotted line is the modeled result for an electrostatic cantilever with comparable geometry.

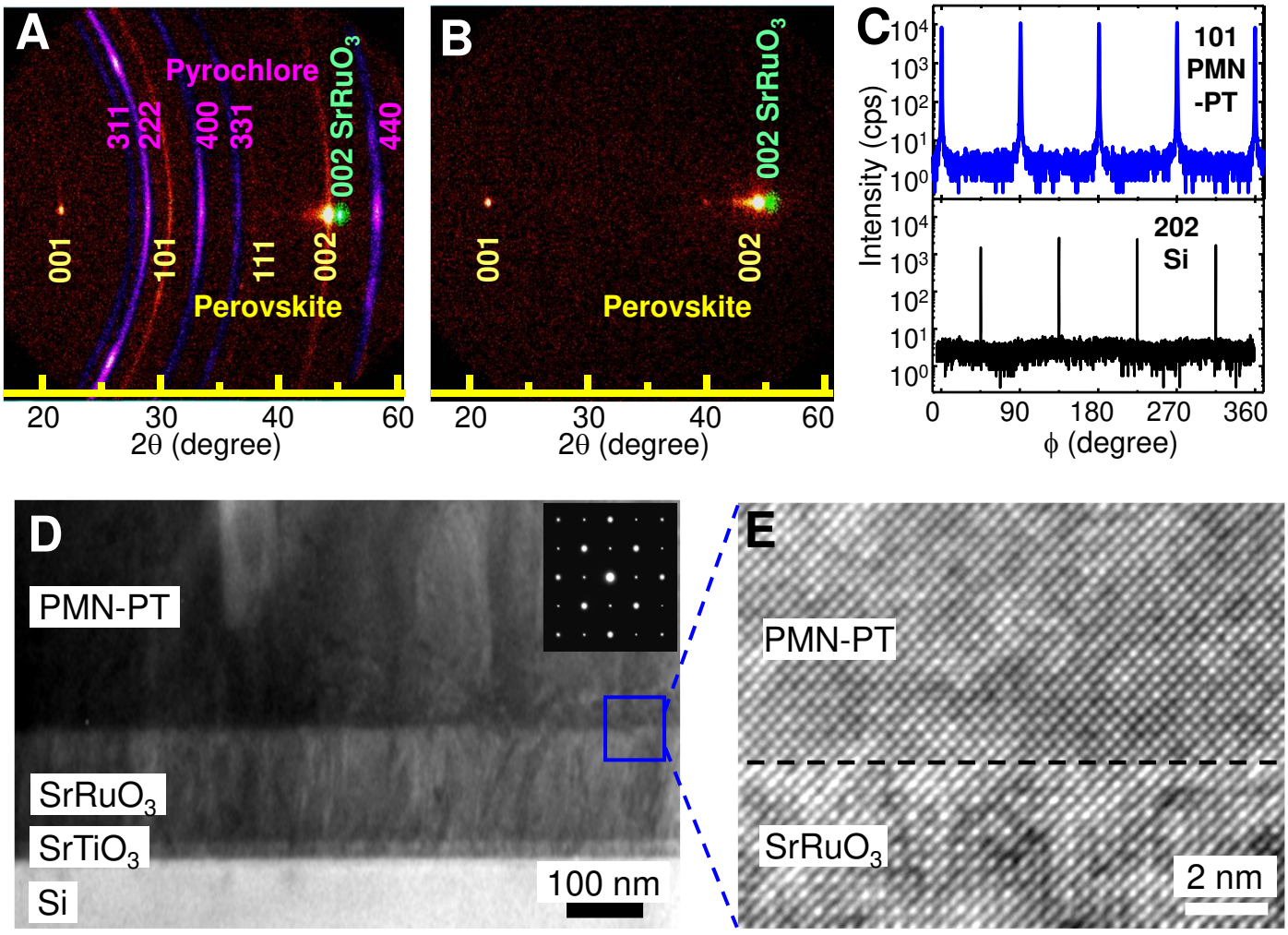

Fig. 1
Baek et al.

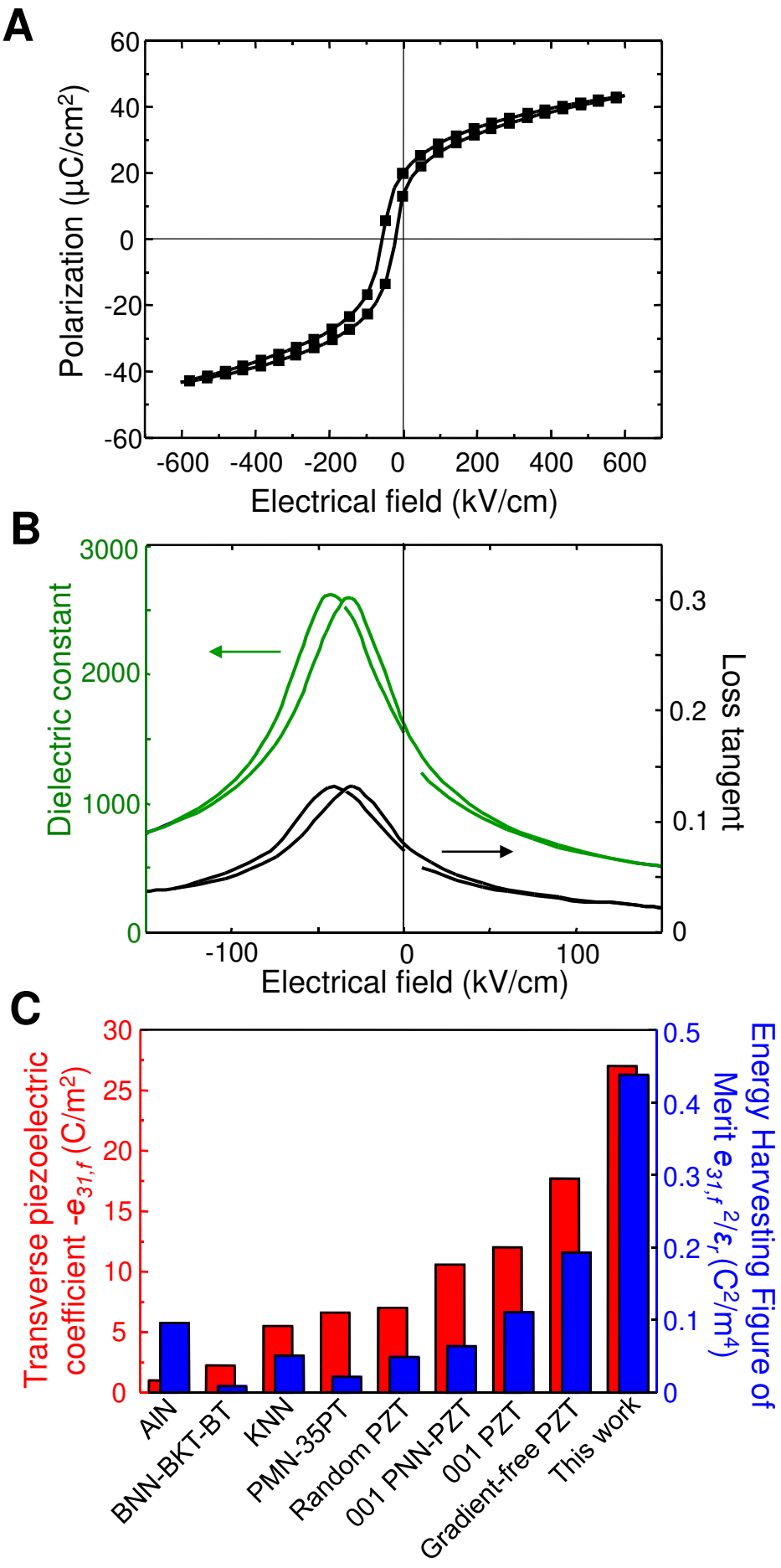

Fig. 2
Baek et al.

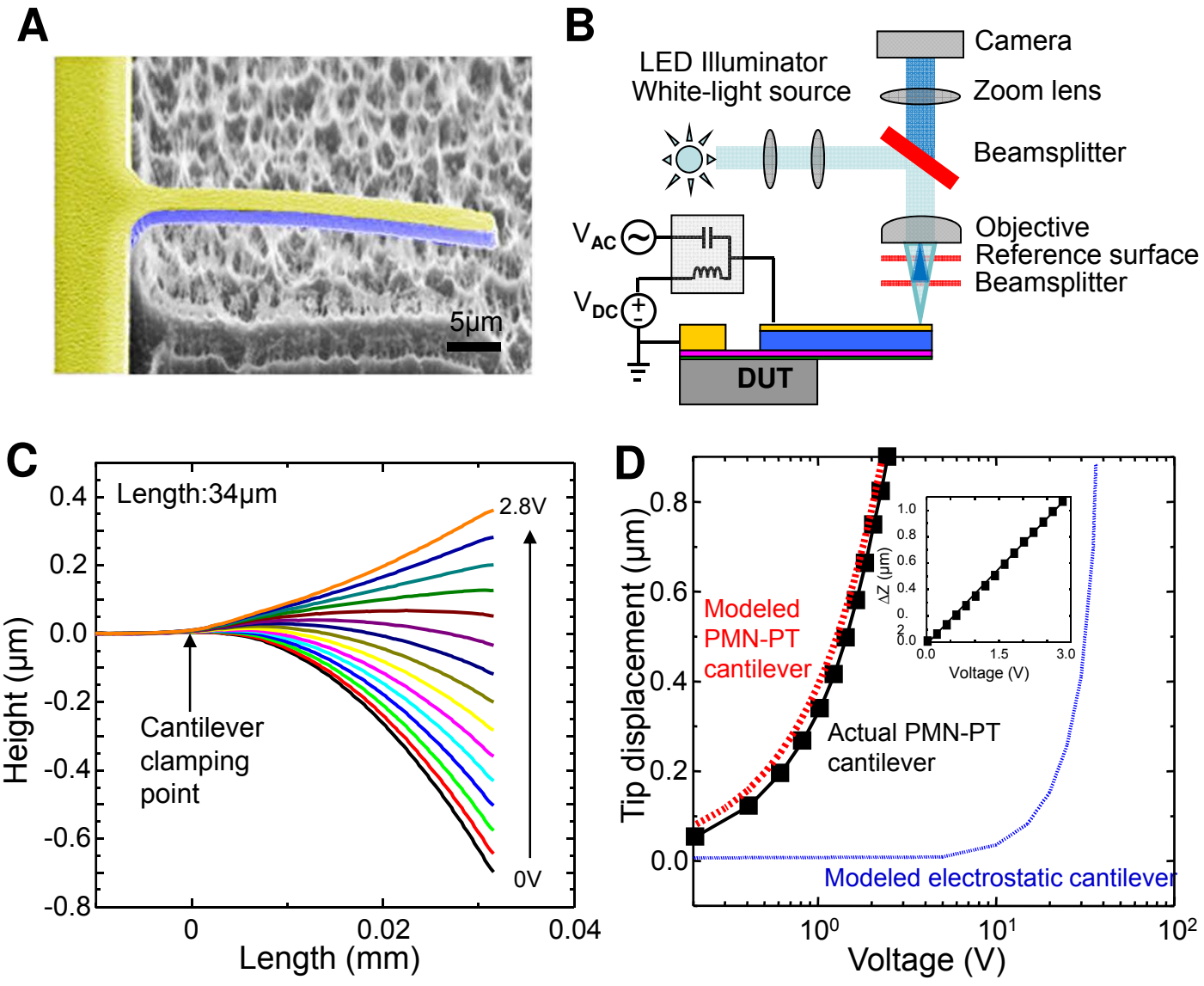

Fig. 3
Baek et al.

Supporting Material

Giant piezoelectricity on Si for hyper-active MEMS

S. H. Baek[1], J. Park[2], D. M. Kim[1], V. Aksyuk[3], R. R. Das[1], S. D. Bu[1], D. A. Felker[4], J. Lettieri[5], V. Vaithyanathan[5], S. S. N. Bharadwaja[5], N. Bassiri-Gharb[5], Y. B. Chen[6], H. P. Sun[6], C. M. Folkman[1], H. W. Jang[1], D. J. Kreft[2], S. K. Streiffer[7], R. Ramesh[8], X. Q. Pan[6], S. Trolier-McKinstry[5], D. G. Schlom[5,9], M. S. Rzchowski[4], R. Blick[2], C. B. Eom[1*]

[1]*Department of Materials Science and Engineering, University of Wisconsin, Madison, WI 53706*

[2]*Department of Electrical and Computer Engineering, University of Wisconsin-Madison, Madison, WI 53706*

[3]*Center for Nanoscale Science and Technology, National Institute of Standards and Technology, Gaithersburg, MD 20899*

[4]*Department of Physics, University of Wisconsin, Madison, WI 53706*

[5]*Department of Materials Science and Engineering, Penn State University, University Park, PA 16802*

[6]*Department of Materials Science and Engineering, University of Michigan, Ann Arbor, MI 48109*

[7]*Center for Nanoscale Materials, Argonne National Laboratory, Argonne, IL 60439*

[8]*Department of Materials Science and Engineering, University of California, Berkeley, CA 94720*

[9]*Department of Materials Science and Engineering, Cornell University, Ithaca, NY 14853-1501*

[*]To whom correspondence should be addressed. E-mail: eom@engr.wisc.edu

$SrTiO_3$ on Silicon Thin Film Growth

Epitaxial $SrTiO_3$ template layers were grown on both exact (001) Si and 4° miscut (001) Si substrates toward [110] using molecular beam epitaxy (MBE) so that the quality of $Pb(Mg_{1/3}Nb_{2/3})O_3$-$PbTiO_3$ (PMN-PT) grown on exact $SrTiO_3$/(001) Si vs. miscut $SrTiO_3$/(001) Si could be compared. The growth method (*41-47*) involves having the oxygen flow only when the substrate is at room temperature, exploiting the kinetic barrier to oxidation of the silicon substrate at low temperature. The incident strontium and titanium are readily oxidized at the relatively high oxygen pressure utilized, but because the substrate temperature is low, the $SrTiO_3$ film thus deposited is amorphous. This amorphous $SrTiO_3$ is subsequently recrystallized through solid-phase epitaxy by heating it in vacuum (*41-47*). Prior work using this method to grow epitaxial $SrTiO_3$/Si showed that the structural quality of the $SrTiO_3$ was degraded as the orientation of the silicon wafers deviated from exact (001) orientation (*43*). For this reason well-oriented (001) Si substrates, cut to within ±0.1° were used in prior studies (*43, 45, 46, 48, 49*).

The signatures in reflection high energy electron diffraction (RHEED) when growing $SrTiO_3$ by the process are different when growing on 4° miscut (001) Si than when growing on well-oriented (001) Si. For example, the intensity vs. coverage of the half-order reconstruction peak traditionally used to terminate the (001) Si surface with one half of a monolayer of strontium (*40, 43, 44, 49*) is completely changed (*47, 50*). Notwithstanding these differences, with accurate calibration it is possible to grow epitaxial $SrTiO_3$ on (001) Si miscut by 4° toward [110]. The crystalline quality of the $SrTiO_3$ produced is inferior to that of the $SrTiO_3$ grown on exact (001) Si. Nonetheless, as Fig. 1 in the main text shows, the PMN-PT grown on top of the miscut $SrTiO_3$/Si is drastically superior due to shorter terrace length on miscut Si.

PMN-PT Thin Film Growth

An epitaxial $SrRuO_3$ layer of 100 nm thickness was deposited as a bottom electrode on $SrTiO_3$–buffered Si substrates by 90° off-axis sputtering at a substrate temperature of 550 °C (*51, 52*). 26.7 Pa (200 mTorr) was maintained during deposition with a 3:2 ratio of Ar and O_2 gases. PMN-PT thin films were grown on top of the $SrRuO_3$ bottom electrode by off-axis sputtering at 630 °C at a sputtering rate of ≈1 μm/hr. A mixture of Ar and O_2 gas with a 17:3 ratio was used with total background pressure of 66.7 Pa (500 mTorr). The 0.67PMN-0.33PT sputtering target has 5 % excess of lead oxide (PbO) in order to compensate the volatile PbO species. Pt is deposited for top electrode at room temperature by on-axis sputtering and patterned by lift-off process.

Cantilever fabrication procedures

A blanket PMN-PT heterostructure (figure S1a) was fabricated with the following thicknesses for each layer of the stack: Pt (60 nm) / PMN-PT (270 nm) / $SrRuO_3$ (100 nm) / $SrTiO_3$ (13 nm) / (001) Si substrate. Then, the Pt and PMN-PT layers were ion-milled to expose the $SrRuO_3$ using S1813 photoresist as a mask. The Ar^+ ion-milling was conducted at etch rates of ≈50 nm/min for Pt, ≈30 nm/min for PMN-PT, and ≈15 nm/min for $SrRuO_3$. The sample was cooled to ≈190 K during etching to prevent burning of the photoresist. Pt bottom electrode contact pads were patterned using a lift-off process as shown in figure S1b. To define the active regions (cantilevers or beams), ion-milling was performed with thicker photoresist (S1827) as a mask until the Si substrate was exposed as shown in figure S1c. An inductively coupled plasma (ICP) etch with 0.93 Pa (7 mTorr) SF_6:O_2 =1:1 was used to etch Si for 30 min. The plasma

etches Si from the exposed silicon side walls, releasing the PMN-PT cantilevers (Figure S1d). Note that this plasma etching does not attack the other layers significantly during Si undercut.

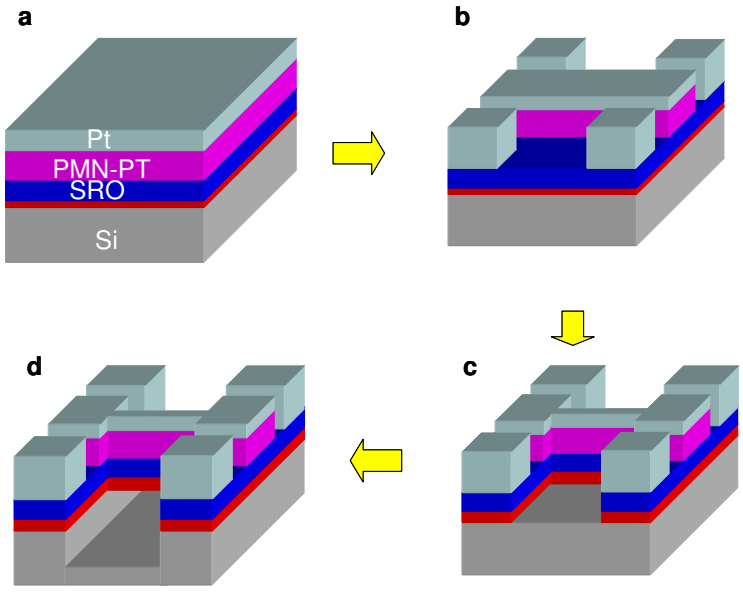

Fig. S1. Microfabrication process for cantilevers or beams. **a,** Epitaxial PMN-PT heterostructure on Si substrate. **b,** Fabrication of bottom electrodes contact pads with Pt. **c,** Ion-milling to define active areas (cantilevers or beams). **d,** Plasma etching to undercut the Si.

Resonance frequency measurements on PMN-PT cantilevers

The resonance frequency of the fundamental mode was measured on various lengths of PMN-PT cantilevers by observing the cantilever deflection with a strobed white light interferometer. A sine wave of 50 mV peak to peak was applied without DC bias and the frequency was changed until the resonance was found. The resonance frequency was independent of voltage amplitude for voltages below 50 mV. The error is less than ±0.5 kHz,

limited by the mechanical quality factor of the cantilever resonance in ambient air, with the typical full width at half maximum (FWHM) peak width of 4 kHz. All measured cantilevers have the similar dimensions except for length. The resonance frequency scales as 1/length^2 as shown in figure S2. Those measured cantilevers are distributed side by side along 1.5 mm long line. This excellent fitting indicates that our PMN-PT films are homogeneous in terms of thickness and composition of PMN-PT, which is also confirmed by wavelength dispersive spectroscopy (WDS). The resonance frequency is an indicator of cantilever stiffness; it was used to correct for discrepancies between modeled and measured cantilever deflection as discussed below.

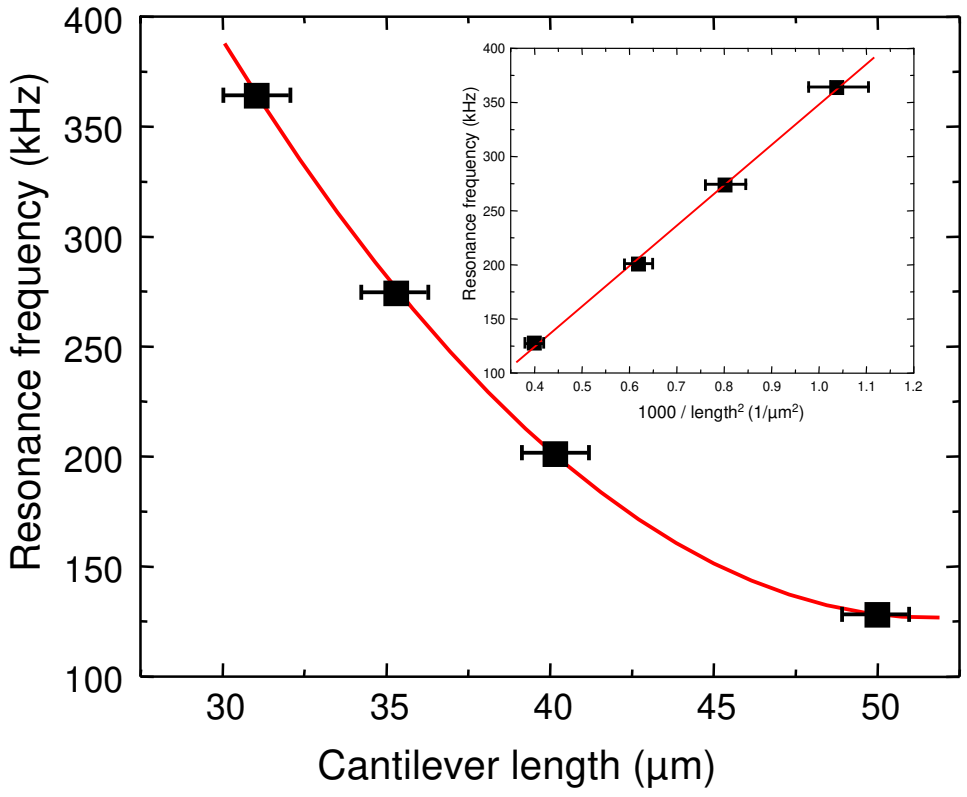

Fig. S2. Resonance frequency versus cantilever length. The inset is resonance frequency versus 1/length^2.

Modeling for Piezoelectric Cantilevers

The mechanical and piezoelectric behavior was modeled using a commercial finite element package. The model contained all the material layers of the real cantilevers. The mesh in figure S3 consisted of parabolic bricks with at least two brick layers for each material layer. The bricks had a lateral size of less than 1 μm over the cantilever area. When we repeated one of the finite element simulations with the mesh elements at one half the linear size in all directions the resonance frequency result was the same within ±1 %, confirming sufficient mesh density for small numerical error. We have used the same cantilever geometry and thickness as our PMN-PT cantilever shown in figure 3a. The material parameters used were shown in Table S1. Piezoelectric (d_{15}=146.1 pC/N, d_{31}=1335 pC/N and d_{33}=2820 pC/N) and stiffness coefficient of the PMN-PT used in the simulation were taken from single crystal PMN-0.33PT (*25*).

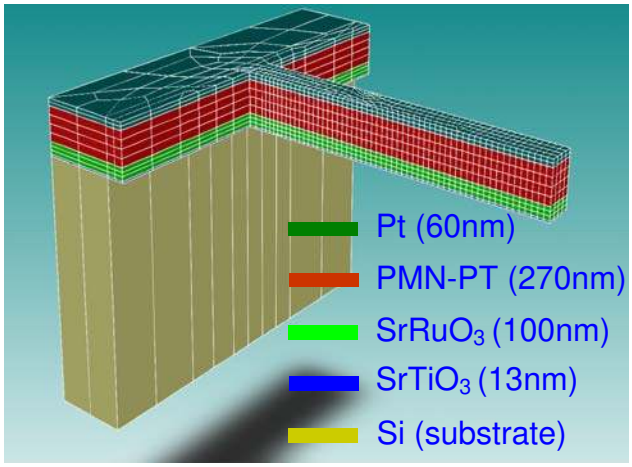

Fig. S3. Cantilever structure of finite element simulation. The model is stretched 5x in the direction normal to the cantilever plane for clarity.

Table S1. Parameters of each layer's mechanical property.

Materials	**Thickness (nm)**	**Density (kg/m^3)**	**Young's modulus (GPa)**	**Poisson's ratio**
Pt	60	21090 (*53*)	168 (*53*)	0.38 (*53*)
PMN-PT	270	8038.4 (*25*)	Full matrix in Ref. 25.	Ref 25.
$SrRuO_3$	100	6489*	161 (*54*)	0.34** (*54*)
$SrTiO_3$	13	5120*	c_{11}=336, c_{12}=107 (*55*)	0.242** (*55*)

*: Theoretical calculation.

**: Calculated values based on data in the reference.

Initial stresses and strains were assumed to be zero with zero electric field applied. Note that the electric field in the z direction is specified as a fixed voltage between the Pt and SRO

layers. Accordingly, four quantities were calculated as shown in Table S2. The numerical error is estimated at ±1 % or less for all values.

(1) The tip displacement, Z, with F = 0.1 μN of mechanical force applied to the cantilever tip at zero voltage applied. It was assumed that the electric field is zero everywhere in the cantilever.

(2) The cantilever stiffness is estimated as F/Z.

(3) Tip displacement with 1 V across the PMN-PT layer. Displacement is a linear function of the applied voltage under the elastic assumptions with fixed piezoelectric coefficients.

(4) The lowest resonance frequency (fundamental mode). It was assumed that electric field is zero everywhere in the cantilever.

Table S2. Simulated cantilever characteristics.

Quantities	Calculated value
Z (μm) under 0.1 μN	0.517
Stiffness (N/m)	0.193
Z (μm) under 1 V	0.70
f_1 (kHz)	205

The simulation results of 0.70 μm/V and f_1= 205 kHz differ from the experimental data of 0.375 μm/V and f_1= 274 kHz. This indicates that the actual cantilever is stiffer compared to the model. This discrepancy might arise from differences in the elastic coefficients between the reported value from bulk materials and our thin films. Assuming the model estimates correctly the cantilever mass per unit length, the actual cantilever is a factor of $(274 / 205)^2 = 1.79$ stiffer

than the model. Given the same piezoelectric bending moment as in the model, the experimental cantilever then would be expected to move (0.70 μm/V) / 1.79 = 0.391 μm/V, which agrees well with the displacement measurement of PMN-PT cantilever.

Modeling for electrostatic cantilevers

The modeled electrostatic displacement vs. applied voltage data describes the displacement at the tip of the cantilever obtained by finite element modeling of the cantilever. The modeling was done by a commercial FEM package solving 3D mechanical and electrostatic problems simultaneously. The cantilever consists of the same material layers with the same mechanical characteristics as was used for the piezoelectric modeling.

For calculating the electrostatic force a DC voltage was applied between the bottom face of the cantilever and a fixed electrode. The fixed electrode is slightly wider than the cantilever and located 2 μm below the cantilever bottom face. The width and length of the cantilever is 3.2 μm and 35 μm, the width and length of the electrode are chosen 6 μm x 37 μm such that making the electrode wider or longer would not significantly change the electrostatic force. The gap between the electrode and the cantilever is chosen so that the DC electrostatically-actuated displacement under constant applied voltage can be stably controlled in the range of 0 μm to 1 μm by changing the voltage. The simulation confirms that displacements of up to 0.88 μm can be stably achieved with voltage under 37 V.

Practically speaking it can be seen from the electrostatic displacement vs. voltage plot that displacements above 0.7 μm become more difficult to control accurately, requiring much finer voltage control, because of the rapid change in displacement as a function of applied voltage. This is a typical situation in these types of electrostatic actuators and is explained by the

nonlinear dependence of the electrostatic force on the actuator position. Displacements above 0.88 μm could not be stably achieved in the simulation.

The choice of the gap between the fixed electrode and the cantilever is dictated by the tradeoff, common in electrostatic actuation, between actuation voltage and the stable range of motion that can be achieved by voltage control without feedback. Larger gap affords larger controllable displacement at the expense of the higher voltage required to reach a given displacement. In this specific case the gap was chosen to afford about 0.9 μm range of motion with the smallest voltage possible. It turned out to be about 36 V.

Imprint of PMN-PT thin film

We have studied to identify the origin of the imprint in PMN-PT thin films by using different electrode configurations and geometries. Figure S4 shows *P-E* hysteresis loop using both symmetric interdigitated electrodes (IDE) on top of PMN-PT thin film and Pt/PMN-PT/$SrRuO_3$ trilayer sandwich structures with asymmetric electrode. The detailed information about IDE fabrication was published in Ref. 56. *P-E* hysteresis loop using IDE shows a symmetric shape without imprint in contrast to very strong imprint in the trilayer structure. Thus, it is believed that the asymmetric nature of top and bottom electrodes plays an important role for the imprint in our PMN-PT thin films (*57, 58*). Additional sources of the asymmetry could be aligned defect dipoles, or possibly strain gradients.

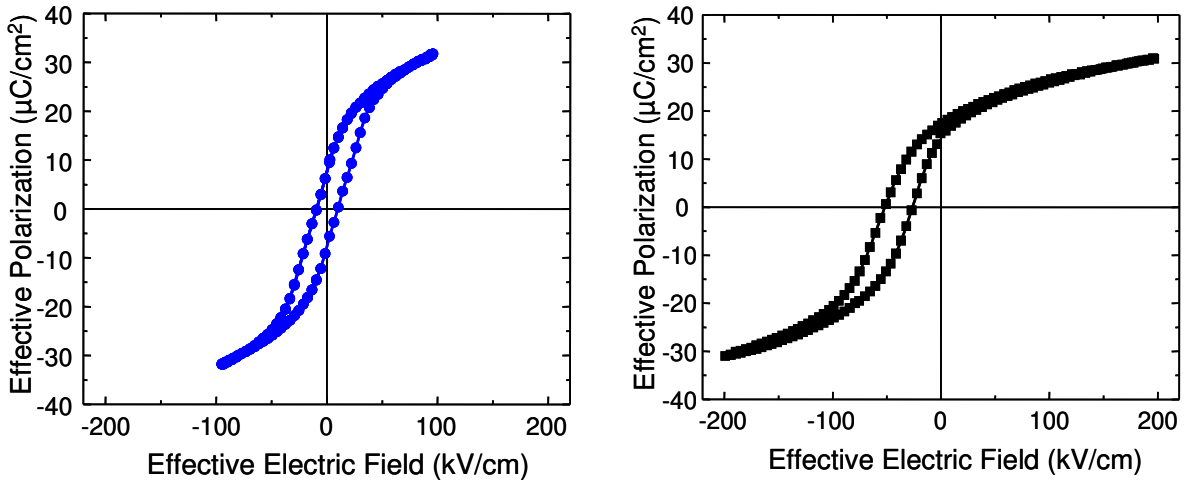

Fig. S4. *P-E* hysteresis loop using symmetric inter digitated electrode (IDE) on PMN-PT thin film and Pt/PMN-PT/$SrRuO_3$ with asymmetric electrodes.

Comparison with PZT by simulation

As piezoelectric device structures vary widely in geometry, comparison can be confusing without appealing to a standard such as a figure of merit. This was our intent in Fig. 2C and the accompanying discussion. However we agree with the referee that a direct comparison of a PZT heterostructure and PMN-PT heterostructure can be informative. To this end, we have numerically modeled the performance of actuator cantilevers with the same dimensions, incorporating our PMN-PT thin films, or PZT films with the piezoelectric properties of PZT-8, and have also numerically modeled PMN-PT and PZT end-loaded cantilevers for energy harvesting.

Using finite element modeling (Coventorware 2008), we have numerically modeled the performance of actuator cantilevers with the same dimensions, when the commonly available thin film PZT piezoelectric material (which has properties similar PZT-8) is substituted for PMN-PT. Table S3 is the result together with the PMN-PT values reported in Table S2 of the supplementary information:

Table S3. Simulated cantilever characteristics.

Quantities	Calculated value, PMN-PT	Calculated value, PZT-8
Z (μm) under 0.1 μN	0.517	0.437
Stiffness (N/m)	0.193	0.229
Z (μm) under 1 V	0.70	0.224
f_1 (kHz)	205	226

Note that while the stiffness increased by 20% (and the frequency correspondingly by 10%), the actuator stroke decreased by over a factor of 3.1 at the same voltage. Thus the PMN-PT actuator is capable of producing about a factor of 2.6 more work.

In order to simulate the energy harvesting characteristics in end-loaded cantilevers, Finite element modeling using Comsol Multiphysics was undertaken. The active piezoelectric layer

dimensions were (length × width × thickness): 2 mm × 0.2 mm × 1 micron on a silicon layer of thickness: 20 microns. The silicon proof mass dimensions are: 0.2 mm × 0.2 mm × 0.2 mm. As a first approximation, the electrodes were presumed to be of negligible thickness. A comparison of the results for an oriented PZT and PMN-PT end-loaded cantilevers for energy harvesting systems are shown in Table S4. It is apparent that the PMN-PT offers substantially higher power levels, as described in the text of the manuscript.

Table S4. Simulated cantilever characteristics.

Quantities	**PMN-PT** ($e_{31,f}$ **= -25 C/m^2**)	**PZT** ($e_{31,f}$ **= -10 C/m^2**)	**PZT** ($e_{31,f}$ **= -17.7 C/m^2**)
Peak Power Density at f_r per "*g*" (mW/cm^2/*g*)	9.17	1.51	4.73
Load (kΩ)	3.9	5.9	5.9
Peak Power at f_r	0.359	0.059	0.185

These ratios between the predicted peak powers for the different piezoelectric films are similar to the ratios of the figures of merit.

References

41. R. A. McKee, F. J. Walker & M. F. Chisholm *Phys. Rev. Lett.* **81**, 3014-3017 (1998).

42. R. A. McKee, F. J. Walker *U. S. Patent* No. 5,830,270 (3 November 1998)

43. J. Lettieri *Critical Issues of Complex, Epitaxial Oxide Growth and Integration with Silicon by Molecular Beam Epitaxy*. http://etda.libraries.psu.edu/theses/approved/WorldWideIndex/ETD-202/index.html (Pennsylvania State University, University Park, 2002).

44. F. J. Walker & R. A. McKee. *High Dielectric Constant Materials: VLSI MOSFET Applications.* 607-637 (Springer, Berlin, 2005).

45. J. Q. He *et al.*, *J. Appl. Phys.* **97**, 104921 (2005).

46. L. V. Goncharova *et al., J. Appl. Phys.* **100**, 014912 (2006).

47. J. W. Reiner *et al., Adv. Mater.* **22**, 2919-2938 (2010).

48. M. P. Warusawithana *et al., Science* **324**, 367-370 (2009).

49. J. Lettieri, J. H. Haeni, D. G. Scholm, *J. Vac. Sci. Technol. A* **20**, 1332-1340 (2002).

50. J. W. Reiner, K. F. Garrity, F. J. Walker, S. Ismail-Beigi, C. H. Ahn, *Phys. Rev. Lett*. **101**, 105503 (2008).

51. C. B. Eom *et al., Science* **258**, 1766 (1992).

52. C. B. Eom *et al., Appl. Phys. Lett.* **63**, 2570 (1993).

53. *Technical data for Platinum*, http://www.periodictable.com/Elements/078/data.html.

54. S. Yamanaka *et al*., *J. Solid State Chem.* **177**, 3484-3489 (2004).

55. N. A. Pertsev, A. K. Tagantsev, N. Setter, *Phys. Rev. B* **61**, R825-R829 (2000).

56. C. M. Folkman *et al., Appl. Phys. Lett.* **96**, 052903 (2010).

57. S. Aggarwal *et al*., *Appl. Phys. Lett.* **69**, 2540-2542 (1996).

58. J. Lee. *et al*., *Appl. Phys. Lett*. **72**, 3380-3382 (1998).